ISSN 0015-4628, Fluid Dynamics, 2019, Vol. 54, no. 3, pp. 374–388. © Pleiades Publishing, Ltd., 2019.
Russian Text © The Author(s), 2019, published in Izvestiya RAN. Mekhanika Zhidkosti i Gaza, 2019, No. 3, pp. 83–97.

Process of the Formation of Internal Waves Initiated by the Start of Motion of a Body in a Stratified Viscous Fluid

P. V. Matyushin

Institute for Computer Aided Design of the Russian Academy of Sciences, Moscow, Russia

e-mail: pmatyushin@mail.ru

Received April 11, 2018; revised October 16, 2018; accepted October 18, 2018

Abstract—The mechanism of formation of three-dimensional internal gravity waves initiated by the start of motion of a disk of given diameter and finite thickness in the horizontal direction along the disk symmetry axis from right to left at a given uniform velocity in an incompressible viscous linearly density-stratified fluid is first considered in detail. The consideration is carried out on the basis of numerical solution of the system of Navier–Stokes equations in the Boussinesq approximation and visualization of the three-dimensional vortex structure of the flow calculated. The obtained fields of the velocity vectors and pressure perturbations possess horizontal and vertical symmetry planes passing through the disk symmetry axis. The process of formation of flow in the upper half-space caused by the shear and gravitational instabilities is described. In this process, two horizontal vortex filaments are initially formed between the back disk face and the place of pulsed start and then transformed into legs of the hairpin vortex loop whose head is located to right of the start point. Thereafter, vortex rings are periodically formed above the start point during half the buoyancy period of fluid. The left-hand halves of the rings are transformed into half-waves occupying space between the disk and the start point.

Key words: stratified viscous fluid, disk, internal gravity waves, mathematical simulation

DOI: 10.1134/S0015462819020095

From both practical and theoretical points of view it is of importance to understand physics of complex three-dimensional processes of generation of spatial internal gravity waves initiated by the motion of bodies in the horizontal direction in a stably stratified viscous continuous medium of the ocean and atmosphere. It is well known that the start of motion of a body is accompanied by emission of time-dependent internal gravity waves propagating along radius-vectors from the start point Q of the body [1, 2].

In the present study, the complex three-dimensional mechanism of formation of the waves initiated by the start of motion of a disk of diameter d and thickness $h = 0.76d$ in the horizontal direction along the axis of symmetry Z from right to left is first considered in detail using the mathematical simulation of flows of an incompressible viscous fluid linearly stratified in density and the visualization of the spatial vortex structure of the flows calculated. The motion occurs at a velocity U for $0.5 < \mathrm{Fr} < 4$ and $\mathrm{Re} = 50$, where $\mathrm{Fr} = UT_b/(2\pi d)$ is the internal Froude number, $\mathrm{Re} = Ud/\nu$ is the Reynolds number, and T_b and ν are the buoyancy period and the kinematic viscosity coefficient of fluid, respectively. In [3] the initial stage of this mechanism in the vertical plane of symmetry of flow is described for $\mathrm{Fr} = 1$ and $\mathrm{Re} = 500$ at $T < 0.5$, where T is time passed from the disk start and nondimensionalized by means of the T_b.

Traditionally, the experimenters when investigating stratified viscous fluid flows consider the internal gravity wave pattern and the wake behind traveling bodies (spheres and cylinders) [2, 4–7] or obstacles on the ground surface [8] only in the vertical plane, whereas the mathematical simulation gives the three-dimensional vortex structure of the internal waves [3, 9–11]. The mechanism of formation of this structure is not investigated experimentally. In [10] a classification of stratified viscous fluid flows past a sphere, which is in adequate agreement with the experiment [6], is given at $0.005 < \mathrm{Fr} < 100$ and $1 < \mathrm{Re} < 500$. The results [12] for the sphere at $\mathrm{Re} = 200$ and $0.125 < \mathrm{Fr} < 100$ are in adequate agreement with the experiment [6] at $0.25 < \mathrm{Fr} < 100$. When $\mathrm{Fr} < 0.25$ in [6] time-dependent periodic flow was observed in the sphere wake, while in [12] steady-state flow was observed. In [11] the flow regimes in the neighborhood of a disk of thickness $h = 0.76d$ were classified for $0.05 < \mathrm{Fr} < 100$ and $50 < \mathrm{Re} < 500$.

The problem of flow induced by diffusion on a sphere placed in a continuously stratified viscous fluid at rest [13] can be used to obtain the initial representation on the three-dimensional mechanism of forma-

tion of spatial internal gravity waves. The flow axisymmetric about the vertical straight line q through the center Q of the sphere was considered. The calculated velocity vector field is also symmetric about the horizontal plane through the point Q. When $T \le 0.5$ an axisymmetric vortex ring which occupies the entire upper half-space is generated here. When $T > 0.5$ a new vortex ring which decreases the vertical dimensions of the rings generated earlier is generated during each $\Delta T = 0.5$ in the neighborhood of the straight line q above the sphere. Each pair the vortex rings forms a single internal gravity wave. The group velocity of these waves is perpendicular to their phase velocity and directed along the radius-vector from each of two effective wave-formation centers, namely, the sphere poles [13]. The wave energy propagates in the radial directions from the sphere poles at the group velocity in parallel to the wave crests. With time, at large distances from the body the phase surfaces with constant angular velocity tend to horizontal planes passing through the wave–formation centers. When $T > 500$ only two vortex rings remain in the neighborhood of these planes. Such vortex rings strongly oblate in the vertical direction are observed experimentally [13].

The two-dimensional problem of uniform motion of an infinitely long horizontal cylinder in the horizontal direction from right to left perpendicularly to its axis of symmetry Z (for $\mathrm{Re} < 200$ and $\mathrm{Fr} < 1$) [2, 3, 9, 10] can also be used to understand the spatial mechanism of formation of internal gravity waves. Here, as in the experiment [13], two wave-formation centers appear in the neighborhood of the point Q at which the cylinder starts to move. In this case, the velocity vector field will be symmetric about the horizontal straight line through the point Q. A new internal wave is generated during each $\Delta T = 1$ in the upper and lower half-planes to right and left of the vertical straight line q through Q [3, 9, 10]. The waves to left of straight line q moves to left together with the cylinder and the waves to right of straight line q remain on the same place being compressed vertically under the action of the waves generated later. The horizontal density gradient isoline patterns in the neighborhood of the square cylinder obtained as a result of the mathematical simulation in [3, 9, 10] at $\mathrm{Fr} = 0.1$ are in very good agreement with the shadow schlieren "vertical slit–Foucault knife" images of flows in the neighborhood of the circular cylinder obtained experimentally [2] at $\mathrm{Fr} = 0.094$.

The present study is the logic continuation of author's studies [3, 9, 10, 13] devoted to an analysis of the mechanism of formation of internal gravity waves.

1. FORMULATION OF THE PROBLEM AND NUMERICAL METHOD

We will consider homogeneous flow of incompressible viscous fluid linearly stratified in density in the horizontal direction Z from left to right at a velocity U. At a certain instant of time a disk of diameter d and thickness $h = 0.76d$ which has the horizontal axis of symmetry Z (Fig. 1a) is instantaneously introduced in this flow and the problem of change in the flow pattern arises. To solve this problem we place the origin of the stationary Cartesian coordinate system (X, Y, Z), where the X axis is vertical, at the geometric center of the disk. The fluid density $\rho(X,Y,Z) = 1 - 0.5X/\mathrm{A} + S(X,Y,Z)$ is nondimensionalized by means of the density ρ_0 at the level of disk center and the coordinates X, Y, Z are nondimensionalized by means of $d/2$; $N = 2\pi/T_b$ and $\Lambda = g/N^2$ are the fluid buoyancy frequency and scale, $\mathrm{A} = \Lambda/d$ is the scale ratio, g is the gravity acceleration, and S is the salinity perturbation nondimensionalized by means of ρ_0 which is equal to zero in the beginning of calculations. The values of the parameter $\mathrm{A} > 100$ were taken to satisfy the conditions $N \approx 1\ \mathrm{s}^{-1}$ and $0.1\ \mathrm{cm} < d < 10\ \mathrm{cm}$ implemented in the experiment.

To simulate mathematically the above problem we solve the system of Navier–Stokes equations in the Boussinesq approximation written in the cylindrical coordinate system (Z, R, φ): $Z = Z$, $X = R\cos\varphi$, $Y = R\sin\varphi$. In the Cartesian coordinate system this system of equations takes the following form:

$$\frac{\partial S}{\partial t} + (\mathbf{v}\cdot\nabla)S = \frac{2}{\mathrm{ScRe}}\Delta S + \frac{v_X}{2\mathrm{A}}, \tag{1.1}$$

$$\frac{\partial \mathbf{v}}{\partial t} + (\mathbf{v}\cdot\nabla)\mathbf{v} = -\nabla p + \frac{2}{\mathrm{Re}}\Delta\mathbf{v} + \frac{\mathrm{A}}{2\mathrm{Fr}^2}S\frac{\mathbf{g}}{g}, \tag{1.2}$$

$$\nabla\cdot\mathbf{v} = 0, \tag{1.3}$$

where $\mathbf{v} = (v_X, v_Y, v_Z)$ is the velocity vector, p is the pressure perturbation nondimensionalized by means of $\rho_0 U^2$, t is time (nondimensionalized by means of $f = d/(2U) = 1/(2\mathrm{Fr}N)$), $\mathrm{Sc} = \nu/\kappa = 709.22$ is the Schmidt number, κ is the salt diffusion coefficient, and ∇ and Δ are the Hamilton and Laplace operators.

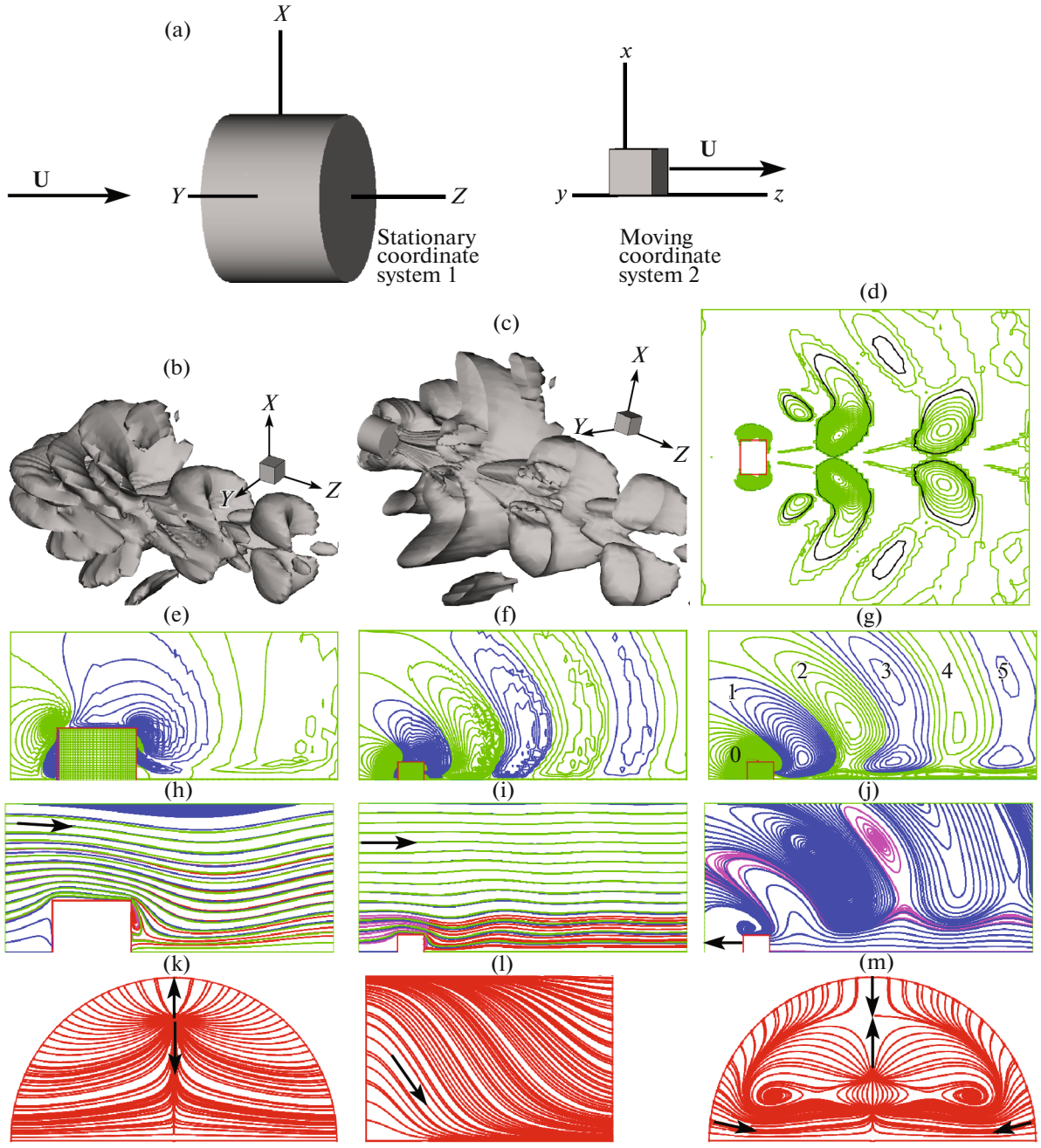

Fig. 1. (a) Formulation of the problem of fluid flow past a disk. (b–m) Visualization of steady-state flow at Fr = 0.5, Re = 50, A = 981.6, and $T = 11.46$ ($C_d = 2.649$) in space (b, c), in the vertical plane X–Z (d–j), and on the disk (k–m): (b, c) isosurfaces for $\beta = 0.02$; (d) β-isolines in steps of 0.01, (e, f) S_z-isolines in steps of 4×10^{-5} and 10^{-5}, (g) S-isolines in steps of 10^{-5}; (h–j) streamlines in the stationary (h, i) and moving (j) Cartesian coordinate systems; and (k–m) skinfriction patterns of the leading (k), lateral (l), and rear (m) disk surfaces in the stationary Cartesian coordinate system.

The solve this problem we used the MERANZh numerical method of splitting in physical factors [14] successfully used for simulation of both incompressible viscous fluid flows past spheres, cylinders, and disks [3, 9–11, 13, 15, 16] and flows with the free surface [14].

The cylindrical computational grid $[Z, R, \varphi] = [I \times J \times K] = [240 \times 110 \times 40]$ occupying the domain $[-13 < Z < 50, 0 < R < 30, 0 < \varphi < 2\pi]$ was used. The grid is concentrated towards all the disk surfaces and

the Z axis so that five grid cells fell on the velocity boundary layer. As the distance from the body surface increases along the Z and R directions, the lengths of the grid cell sides increase monotonically along the Z and R directions, respectively, in accordance with the polynomial law up to a certain maximum and then they do not vary. At Re = 50 the minimum (maximum) grid cell dimensions along the Z and R directions are equal to 0.036 and 0.035 (0.41 and 0.67), respectively.

The staggered grid was used so that the variables S and p were determined at the centers of the computational cells and the velocity components at the centers of their faces; the variables S and p were not determined on the body surface.

We will describe the algorithm of calculations for the Cartesian coordinate system. At the initial instant $t_0 = 0$ a certain initial flow was specified in the neighborhood of the disk. Let at $t_n = n\tau$, where τ is the time step and n are the numbers of steps ($n = 0, 1, 2, 3, ...$), the values of S, $\mathbf{v} = (v_X, v_Y, v_Z)$, and p be known. Then the scheme of finding the unknown functions S, $\mathbf{v}$, and p at the instants of time $t_{n+1} = (n+1)\tau$ can be represented in the form:

$$\frac{S^{n+1} - S^n}{\tau} = -(\mathbf{v}^n \cdot \nabla)S^n + \frac{2}{\mathrm{ScRe}}\Delta S^n + \frac{v_X^n}{2\mathrm{A}}, \tag{1.4}$$

$$\frac{\mathbf{w} - \mathbf{v}^n}{\tau} = -(\mathbf{v}^n \cdot \nabla)\mathbf{v}^n + \frac{2}{\mathrm{Re}}\Delta \mathbf{v}^n + \frac{\mathrm{A}}{2\mathrm{Fr}^2}S^{n+1}\frac{\mathbf{g}}{g}, \tag{1.5}$$

$$\tau \Delta p = \nabla \cdot \mathbf{w}, \tag{1.6}$$

$$\frac{\mathbf{v}^{n+1} - \mathbf{w}}{\tau} = -\nabla p, \tag{1.7}$$

where $\mathbf{w}$ is an auxiliary intermediate velocity.

Addition of Eqs. (1.5) and (1.7) gives Eq. (1.2). Equation (1.6) can be obtained in multiplying the Hamilton operator in the scalar way by Eq. (1.7) with regard to the continuity equation (1.3).

To approximate the convective terms of Eqs. (1.4)–(1.5) we used the hydride finite-difference scheme for which the second order of approximation in spatial variables, the minimum artificial viscosity and dispersion, workability over a wide Re and Fr range, and monotonicity are characteristic [14]. The central differences were used to approximate other spatial derivatives in Eqs. (1.4)–(1.7).

We will now consider the approximation of the Poisson equation (1.6) at the inlet of the outer boundary of the cylindrical computational domain ($Z = -13$)

$$\tau\frac{(p_{2,j,k} - p_{1,j,k}) - (p_{1,j,k} - p_{0,j,k})}{h^2} + \Lambda = \frac{w_{z,2,j,k} - w_{z,1,j,k}}{h} + \Lambda, \tag{1.8}$$

where h is the grid step, $p_{0,j,k}$ and $p_{1,j,k}$ are the pressures at the centers of the cells "0, j, k" and "1, j, k," located to the left and right with respect to the boundary, respectively ($j = 1, 2,..., J$; $k = 1, 2, ..., K$). In (1.8) the boundary values of $p_{0,j,k}$ and $w_{z,1,j,k}$ are unknown.

We will write the expression for $w_{z,1,j,k}$ obtained from Eq. (1.7):

$$w_{z,1,j,k} = v_{z,1,j,k}^{n+1} + \tau\frac{(p_{1,j,k} - p_{0,j,k})}{h}.$$

Substitute this expression for $w_{z,1,j,k}$ in Eq. (1.8)

$$\tau\frac{(p_{2,j,k} - p_{1,j,k})}{h^2} + \Lambda = \frac{w_{z,2,j,k} - v_{z,1,j,k}^{n+1}}{h} + \Lambda. \tag{1.9}$$

Thus, instead of Eq. (1.8), on the inlet part of the outer boundary of the cylindrical computational domain ($Z = -13$) we can use Eq. (1.9), where already there are no unknown boundary values $p_{0,j,k}$ and $w_{z,1,j,k}$. Similarly, we can show that there is no need for the boundary conditions for the pressure on all the remaining boundaries.

On the rigid disk surface we impose the no-slip and no-flow boundary conditions: $\mathbf{v} = (v_z, v_R, v_\varphi) = (0, 0, 0)$ and $\partial\rho/\partial n = 0$, where $\mathbf{n}$ is the normal vector to the disk surface ($\partial S/\partial z = 0$ on the leading and rear disk sides and $\partial S/\partial R = 0.5\cos\varphi/\mathrm{A}$ on the lateral disk side). At the inlet of the outer boundary of the cylin-

drical computational domain ($Z = -13$) we have $\mathbf{v} = (1, 0, 0)$ and $\partial S/\partial z = 0$. On the lateral part of the outer boundary ($R = 30$): $\mathbf{v} = (1, 0, 0)$ and $\partial S/\partial R = 0$. On the rear part of the outer boundary ($Z = 50$): $v_z = 1$, $v_R = 0$, $\partial v_\varphi/\partial z = 0$, and $\partial S/\partial z = 0$. At infinity from the body $S = 0$; however, the "free" boundary conditions $\partial S/\partial n = 0$ are imposed on the outer boundary by virtue of the finite dimensions of the computational grid. It is natural to impose the "free" boundary conditions $\partial v_\varphi/\partial z = 0$ for the third component of velocity vector on the rear part of the outer boundary. Unfortunately, the formulation of similar "free" boundary conditions for all the velocity components at $Z = 50$ leads to abend of the calculation process.

The software created for the mathematical simulation and visualization of three-dimensional stratified viscous flow flows past the disk was thoroughly tested [3, 11]. For Re = Fr = 50 and A = 9816 the disk drag coefficient is equal to $C_d = 1.923$ and the length of the recirculation (stagnant) region D1 downstream of the disk reckoned from the rear stagnation point on the disk is equal to $L/d = 0.741$. This is in adequate agreement with the experiment [17]. The calculations were carried out with the use of computational resources of Joint Supercomputer Center of the Russian Academy of Sciences (JSCC RAS).

2. VISUALIZATION OF THE CALCULATION RESULTS

When Fr > 10 the flow past the disk will be equivalent to a homogeneous viscous fluid flow and represents the body wake in the stationary Cartesian coordinate system. When Fr < 5 generation of internal gravity waves characterized by the horizontal and vertical planes of symmetry passing through the Z axis can be observed [3, 9–11].

We will consider steady-state three-dimensional flow field calculated for Fr = 0.5, Re = 50, and A = 981.6 (Fig. 1) [3, 9–11]. By virtue of the presence of the horizontal Y–Z plane of symmetry, the velocity vector fields of this flow will be analyzed only in the upper half-space.

In Figs. 1k–1m we have reproduced the skinfriction pattern (limiting streamlines) on the disk surface [15, 16] for $X > 0$. The flow incoming from left (Fig. 1a) focuses at a certain point on the leading disk side (nearer to the upper boundary) and then spreads over the leading side in various directions (Fig. 1k). On the lateral disk sides the flow tends downward towards the Y–Z plane (Fig. 1l). By virtue of existence of the vertical X–Z plane of symmetry of the velocity vector field of this flow, we can observe streamlines in the X–Z plane (Figs. 1h–1j). The "sinusoidal" streamline pattern is more visual in the stationary Cartesian coordinate system (Figs. 1h–1i). In this case, the wave crests and hollows can be observed. In Fig. 1i the distance between the first and second wave crests along the Z axis is equal to approximately λ, where $\lambda = UT_b = 2\pi U/N = 2\pi \mathrm{Fr} d$ is the length of internal waves in the X–Z plane.

As a rule, the patterns of isolines of various density derivatives are observed in the experiments. For example, the popular and informative schlieren "vertical slit–Foucault knife" image [2] gives the pattern of isolines of the horizontal density gradient S_z. Below, for comparison with the experiment, the S_z-isolines in the vertical plane X–Z (Figs. 1e–1f) are constructed. In Fig. 1f the dark ($S_z < 0$) and light ($S_z \geq 0$) stripes visualize the phase surfaces of internal waves and the crest and hollow lines, clearly seen in Fig. 1i, are located on their boundaries. In this sense, figures 1f and 1i are similar. At the same time, the field of S_z-isolines in the neighborhood of the rear disk side (Fig. 1e) gives more the structural flow elements than the streamline pattern in Fig. 1h. In Fig. 1g the dark ($S < 0$) and light ($S \geq 0$) stripes on the S–isoline pattern visualize the hollow and crest half-waves, respectively.

Since in the experiments the body usually moves with respect to the fluid at rest, we introduce the second (moving) Cartesian coordinate system (x, y, z) (the x axis is vertical and the z axis is parallel to the Z axis) which moves uniformly from left to right at the velocity U with respect to the first (stationary) Cartesian coordinate system introduced above (Fig. 1a). When the values of the horizontal components of the velocity vectors calculated in the first Cartesian coordinate system decrease by unity then we can observe the streamlines in the moving Cartesian coordinate system (compare Figs. 1h–1i and 1j). The values of the vertical components of the velocity vectors and the variables S and p are the same in the first and second Cartesian coordinate systems.

The instantaneous streamline patterns constructed in the second Cartesian coordinate system visualize the circulation (vortex) flow cells (Fig. 1j). At $t = 0$ the origin of the second Cartesian coordinate system coincides with the center Q of the rear disk side. In time $T = [tf]/T_b = [t/(2\mathrm{Fr}N)][N/2\pi] = t/(4\pi\mathrm{Fr})$ the origin of the second Cartesian coordinate system is displaced at the distance $s = U[tf]/(0.5d) = t = 4\pi\mathrm{Fr}T$ in the first Cartesian coordinate system.

It can be shown [9] that for steady-state flow the S–isoline pattern in the plane of symmetry X–Z (Fig. 1g) is similar to the streamline pattern in the second Cartesian coordinate system (Fig. 1j). In this pattern we

can clearly distinguish the wave-like fluid motion near the Z axis behind the rear disk face which is uniformly moving from right to left and a series of elongated circulating cells above it. We will call the part of fluid in Fig. 1j between the circulating cell of number M and the Z axis by the "base" M of this cell. In the circulation cell 0, adjacent to the disk in Fig. 1j, fluid circulation occurs clockwise, in the next elongated "base" 1, adjacent to the cell 0 from right, fluid describes a loop moving counterclockwise; in cell 2, adjacent to the base 1 from right, fluid circulation is directed clockwise, etc. In Fig. 1g we have plotted the numbers of cells 0 and 2–5 and base 1. Thus, in Fig. 1j fluid circulates clockwise in cells 0, 2, and 4 and counterclockwise in cells 3 and 5 (hollows half-waves). In Figs. 1g and 1j the bases 1, 3, and 5 can be clearly traced.

The function β was determined at each of the centers of computational grid cell to represent the three-dimensional vortex flow structure. If at the center of a cell there exist complex conjugate eigenvalues $\sigma_{1,2} = \alpha \pm i\gamma$ of the velocity gradient tensor $\mathbf{G}$, then $\beta = \gamma > 0$, else $\beta = -1$. Then, the isosurface $\beta = \beta_0 > 0$ is constructed (Figs. 1b, 1c). If at a certain fixed point of flow $\beta > 0$, then in the Cartesian coordinate system $\mathbf{x}$ with the origin at this point which travels at the velocity of this point we can write the ordinary differential equation $\mathbf{v} = d\mathbf{x}/dt \approx \mathbf{G}\mathbf{x}$, where $\mathbf{v}$ is the fluid velocity in the Cartesian coordinate system $\mathbf{x}$. It can be shown [16] that in the Cartesian coordinate system $\mathbf{x}$ the phase trajectory of a liquid particle is a plane spiral along which the particle moves around a taken point of flow at the angular velocity β. The spatial vortex structures of the double-thread wake and the chains of hairpin-shaped vortex loops in the wake behind a sphere in homogeneous viscous fluid flow obtained with the use of β-visualization in [15, 16] are in a good agreement with the vortex structures obtained experimentally [18, 19] by means of dye or emulsion visualization.

The pattern of isolines of $\beta > 0$ plotted in the vertical plane X–Z in Fig. 1d is similar to the streamline pattern plotted in the second (moving) Cartesian coordinate system in Fig. 1j. Each of the half-waves in Figs. 1g and 1j can be put in correspondence to a half-wave in Fig. 1d. Thus, in Fig. 1d we can distinguish three hollow half-waves in the plane X–Z (corresponding to dark stripes 1, 3, and 5 with $S < 0$ in Fig. 1g) and two crest half-waves (corresponding to light stripes 2 and 4).

From Fig. 1d there follows transition from the two-dimensional vortex structure of internal waves in the plane X–Z to the three-dimensional wave structure in Figs. 1b and 1c in which the U-shaped structures of the first hollow and crest half-waves, a fragment of the second hollow half-wave, and the V-shaped structures of the "axial parts" of the first (only in Fig. 1c), second, and third crest half-waves near the Z axis are shown. The latter are related to one another and to D1 by means of the horizontal vortex filaments.

3. EVOLUTION of FLUID FLOW AT $T \le 0.7$

When the disk starts in the horizontal direction in a stably stratified viscous fluid with the density $\rho_{00}(X) = 1 - \dfrac{X}{2A}$, the liquid particles near the disk leave the state of rest and begin to oscillate at the buoyancy frequency N in the vertical direction. These oscillations in the near-wake dump with time, forming internal waves (Fig. 1) which propagate from right to left together with the body at the body velocity in the moving Cartesian coordinate system. In what follows, we will describe the process of formation of these waves in detail.

When Fr = 4 and Re = 50 laminar flow past the disk is observed in the streamline pattern at $T \le 0.001$ in the stationary Cartesian coordinate system. At $T = 0.008$ flow separates in the neighborhood of the rear disk edges and attaches to the rear disk side above the Z axis. Here, the main mechanism of formation of viscous fluid flow 1k operates (generation of the vortex ring (or semiring) in the neighborhood of the body surface) [16]. The numeral 1 in the mechanism name 1k means that this mechanism operates in D1.

In Fig. 2 we can observe regions D1 of length $L/d = 0.388$, 0.565, 0.653, 0.671, and 0.729 at $T = 0.04$, 0.08, 0.12, 0.14, and 0.32, respectively. At $T > 0.32$ the length L/d does not increase, the thickness of D1 in the rear disk side being equal to $0.928d$. When Fr = 4 and Re = 50 the vortex sheet (flow region D2 in Fig. 2d) and D1 are axisymmetric.

If q is a vertical straight line through the point Q of pulsed start of the center of rear disk side, then this center moves to left in the second (moving) Cartesian coordinate system at the distance $s = 4\pi \mathrm{Fr} T$ from the stationary straight line q. When $0.02 < T < 0.04$ four vortex structures which are symmetric about the X–Z and Y–Z planes (right half of Fig. 2b) begin to be formed between the right edge of the sheet and the straight line q at the place of sharp shear of fluid in the neighborhoods of the planes $\varphi = \pi/4$ and $\varphi = 3\pi/4$. In Fig. 2 we have reproduced the further development of these structures at $0.06 \le T \le 0.32$ using both

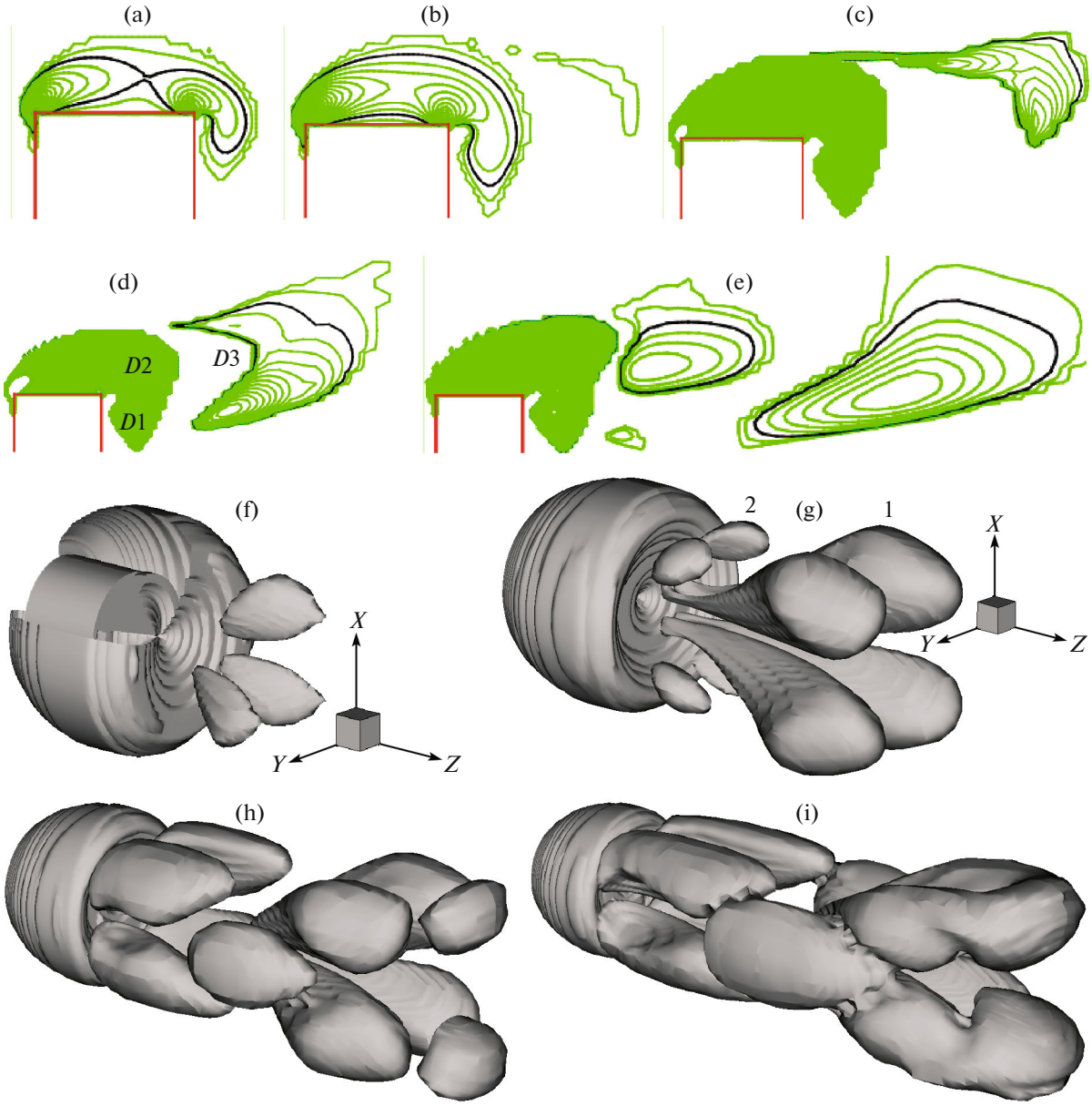

Fig. 2. Flow behind the disk at Fr = 4, Re = 50, and A = 2776.4: (a–e) isolines for $\beta > 0$ at $\varphi = \pi/4$ in steps of 0.2, 0.1, 0.0002, 0.0005, and 0.002 at $T = 0.02$, 0.04, 0.06, 0.08, and 0.19; (f–i) isosurfaces for $\beta = 0.003$ at $T = 0.08$, 0.16, 0.24, and 0.32.

$\beta > 0$-isolines in the planes $\varphi = \pi/4$ (in the right halves of Figs. 2c–2e) and the β-isosurfaces (Figs. 2f–2i). When $T \geq 0.08$ these four structures are already similar to vortex filaments. When $0.04 \leq T \leq 0.19$ (see Figs. 2b–2g) the straight line q passes through the right ends of the first group of four filaments. When $0.14 < T < 0.16$ the left ends of the first group of four filaments (near D1) induce the second group of four vortex filaments (Figs. 2e and 2g). (In Fig. 2g the numerals 1 and 2 mark the first and second groups of four vortex filaments, respectively.)

When $0.22 < T < 0.24$ a single head vortex is induced on the right of each pair of the right ends of the first and second groups of four filaments (Fig. 2h). When $0.3 < T < 0.5$ each of the filament pairs including their head vortex transforms into a hairpin-shaped vortex loop (Figs. 2i and 3a). Thus, the first and second groups of four vortex filaments transform into the first and second pairs of vortex loops, the legs of the second pair of the loops contacting the sheet D2. From Fig. 4d it follows that the fluid rotates clockwise in the cross-section of the head of the first vortex loop by the vertical plane X–Z (cell – 1) when $X > 0$.

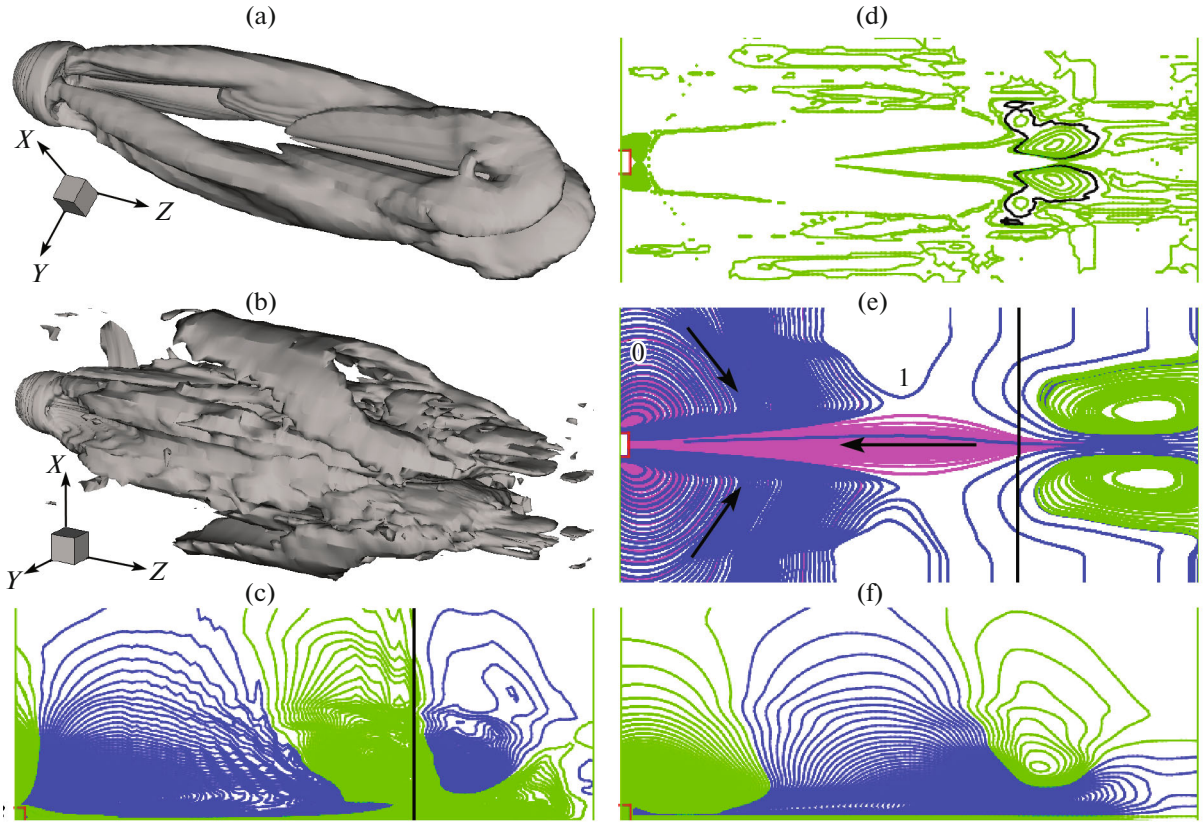

Fig. 3. Flow behind the disk at Fr = 4, Re = 50, A = 2776.4, and $T = 0.72$: (a, b) isosurfaces for $\beta = 0.003$ and 0.001; (c) S_z-isolines in steps of 10^{-7}, (d) β-isolines in steps of 0.001, (f) S-isolines in steps of 10^{-6}, and (e) instantaneous streamlines in the moving Cartesian coordinate system in the vertical plane X–Z.

Consequently, when $X > 0$, $Y > 0$, and $Z > 0$ the fluid rotates counterclockwise in the vertical cross-section of leg of the first vortex loop (when looking at the rear disk side).

In accordance with [16], the detailed mechanism of vortex formation at $T < 0.5$ can be symbolically written as follows: M1 = {2k–1k–3f–3f–3t/b–3r/l}, where 2k denotes the disk sheet formation, numeral 3 denotes flow D3 outside the sheet (Fig. 2d), 3f denotes the generation of four vortex filaments in D3 (initially, the first group of four filaments and then the second group), 3t/b/r/l is the generation of heads of vortex loops oriented upward (t), downward (b), to the right (r) and to the left (l). Formation of these vortex loops (mechanism M1) is caused by the shear and gravitational instabilities of the stratified viscous fluid initiated by the disk motion.

Dynamics of the patterns of instantaneous streamlines in the moving Cartesian coordinate system and S- and S_z-isolines in the vertical plane X–Z at $0.01 \le T \le 0.24$ shown in Fig. 4 supplement the above-described process of vortex loop formation (spatial mechanism M1). At $X > 0$ the start of disk motion forms a single large circulation cell 0 in the pattern of instantaneous streamlines in the moving Cartesian coordinate system, two cells in the pattern of S-isolines (left and right), and three cells in the pattern of S_z-isolines (Fig. 4a). In the S_z–isoline pattern (Fig. 4, II) the straight line q (black vertical line) passes a little to right of the boundary between the central and right cells, i.e., the central cell visualizes the path passed by the body in the moving Cartesian coordinate system. In the S–isoline pattern (Fig. 4, III) the right cell is also displaced to right at $0.01 < T < 0.24$. On basis of S– and S_z–isoline patterns it is not possible to understand the flow evolution mechanism visually shown by instantaneous streamlines in the plane X–Z. Intensive clockwise fluid rotation to the left of the straight line q leads to formation of circulation cell 1 to right of q (with counterclockwise fluid rotation in Fig. 4c), which, in its turn, induces (together with the right ends of the first group of four vortices in Fig. 2h) formation of circulation cell –1 (head of the first vortex loop) near the Z axis to right of q (Fig. 4d).

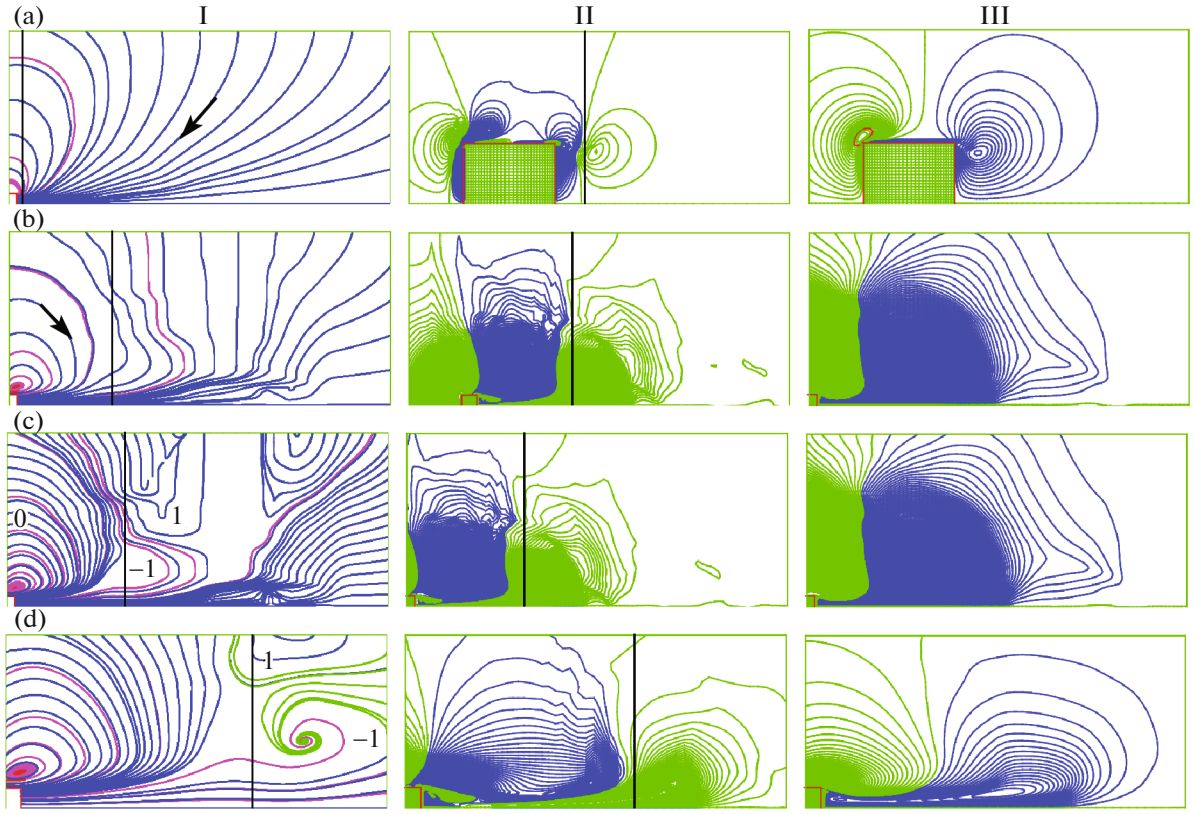

Fig. 4. Flow behind the disk at Fr = 4, Re = 50, and A = 2776.4 in the vertical plane X–Z: (a–d) instantaneous streamlines in the moving Cartesian coordinate system (I), $S_\nu \times 10^6$ isolines in steps of 10, 0.1, 0.1, and 1 (II), and $S \times 10^6$ isolines in steps of 3, 0.1, 0.1, and 5 (III) at T = 0.01, 0.19, 0.22, and 0.24.

When $0.25 \le T \le 0.7$ the disk together with zeroth cell is displaced to left making room for approaching cell 1 to the Z axis (Fig. 3e), i.e., the first hollow half-wave is formed from cell 1 to left of straight line q (Fig. 3f).

When $0.4 \le T \le 0.7$ the heavier fluid rises along the straight line q to the equilibrium level for the lighter fluid on the boundary between circulation cells 1 (with counterclockwise fluid circulation) and −1 (with clockwise fluid circulation). Therefore, in the neighborhood of line q negative values of S become positive and when $0.4 \le T \le 0.7$ a certain new light cell with $S > 0$ (Figs. 3f and 5a–5b (III)) descends along the straight line q in the S–isoline pattern. In Fig. 4d (III) this cell divides the right cell with $S < 0$ into cell 1 (to left of q) and cell −1 (to right of q). Thus, in the S–isoline patterns the cells 1 and −1 are formed later than the circulation cells 1 and −1 in the instantaneous streamline patterns and at $0.4 \le T \le 0.7$ formation of the first and second pairs of vortex loops is accompanied by formation of the first hollow half-wave.

The same spatial mechanism M1 operates also at Fr = 0.5 (Figs. 5a–5b and 6a–6e). Though at the same T the path $s = 4\pi \mathrm{Fr} T$, passed by the disk in the moving Cartesian coordinate system at Fr = 0.5, will be by 8 times shorter than the path at Fr = 4. We could assume that at Fr = 0.5 the flow patterns can be obtained from the patterns at Fr = 4 by means of their simple horizontal contraction by 8 times. But in fact this is not exactly so. For example, when $0.25 \le T \le 0.6$ strong fluid rotation in the circulation cell −1 (head of the first loop) (Figs. 5a–5b (II)) generates the high base 1 of the first hollow half-wave, while the circulation cell 1 cannot already be seen above the base 1. At the same time, when $0.01 < T < 0.1$ the first group of four vortices is generated adjoining the vortex sheet (Figs. 6a–6b). Therefore, when $0.14 < T < 0.16$ the second group of four vortices is already formed in the neighborhood of the lateral disk sides (Fig. 6c).

When $0.24 < T < 0.25$, at Fr = 0.5 the heads come into being ahead of the first group of four vortices (Fig. 6d). At Fr = 0.5 the heads of the second group of four vortices are not seen in Fig. 6d. Thus, when $T \le 0.7$ the stages of formation of the first pair of vortex loops depend only slightly on Fr at $0.5 \le \mathrm{Fr} \le 4$ and are determined by only the instant of time T.

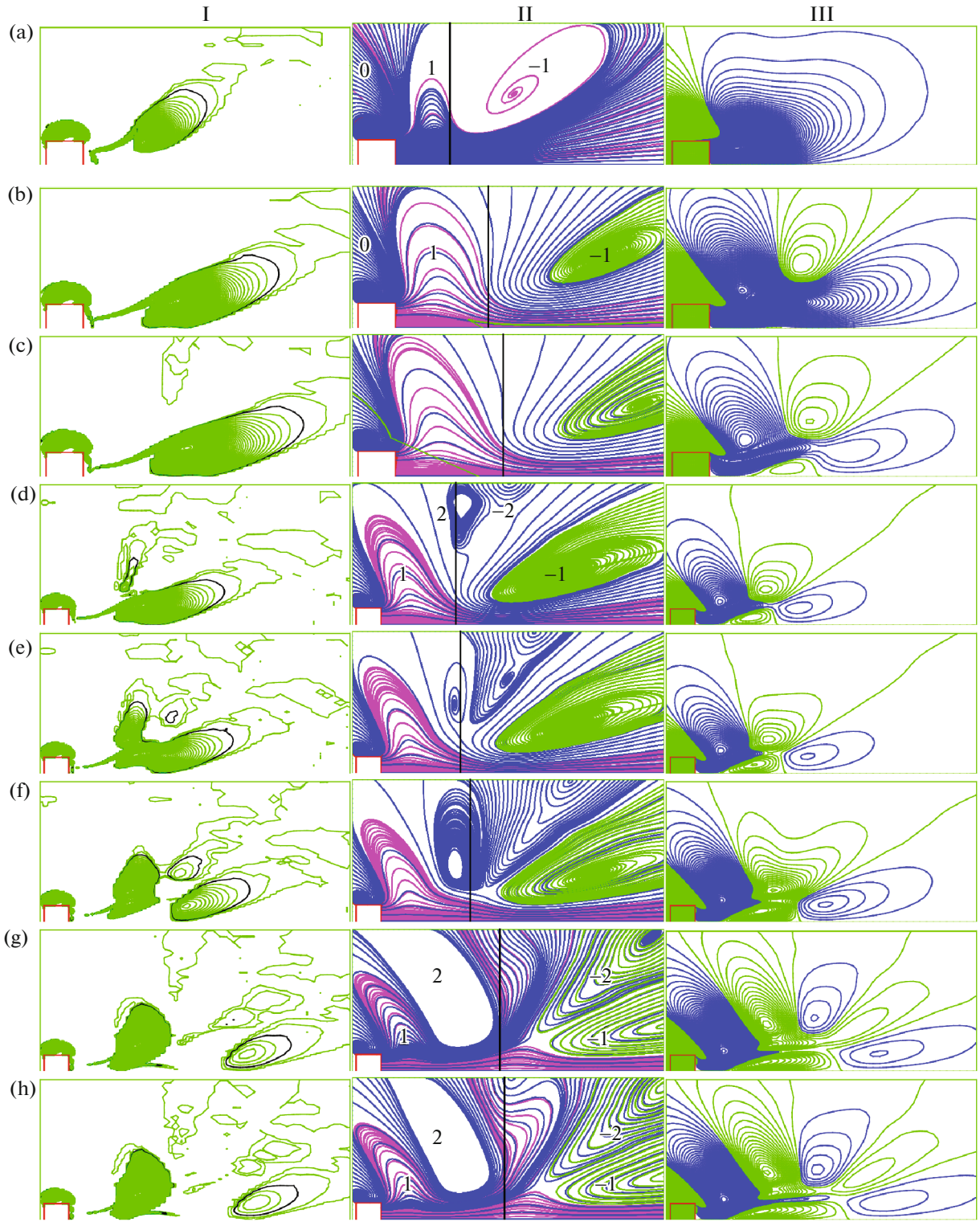

Fig. 5. Flow behind the disk at Fr = 0.5, Re = 50, and A = 981.6 in the plane X–Z: (a–h) β-isolines in steps of 0.002 (I), instantaneous streamlines in the moving Cartesian coordinate system (II), and $S \times 10^6$ isolines in steps of 2, 2, 6, 6, 6, 3, 3, and 3 (III) at $T = 0.35$, 0.6, 0.7, 0.75, 0.8, 0.9, 1.2, and 1.25.

4. EVOLUTION OF FLUID FLOW AT $T > 0.7$

When $0.25 < T < 0.8$ the head of the first loop is formed around the straight line q (Figs. 6d and 6e). In Figs. 5a–5e (II) the head includes the circulation cells 1 and −1. We will consider it as the first vortex semiring. When $0.6 < T \le 0.7$ the upward vortex-free fluid motion can be observed on the boundary

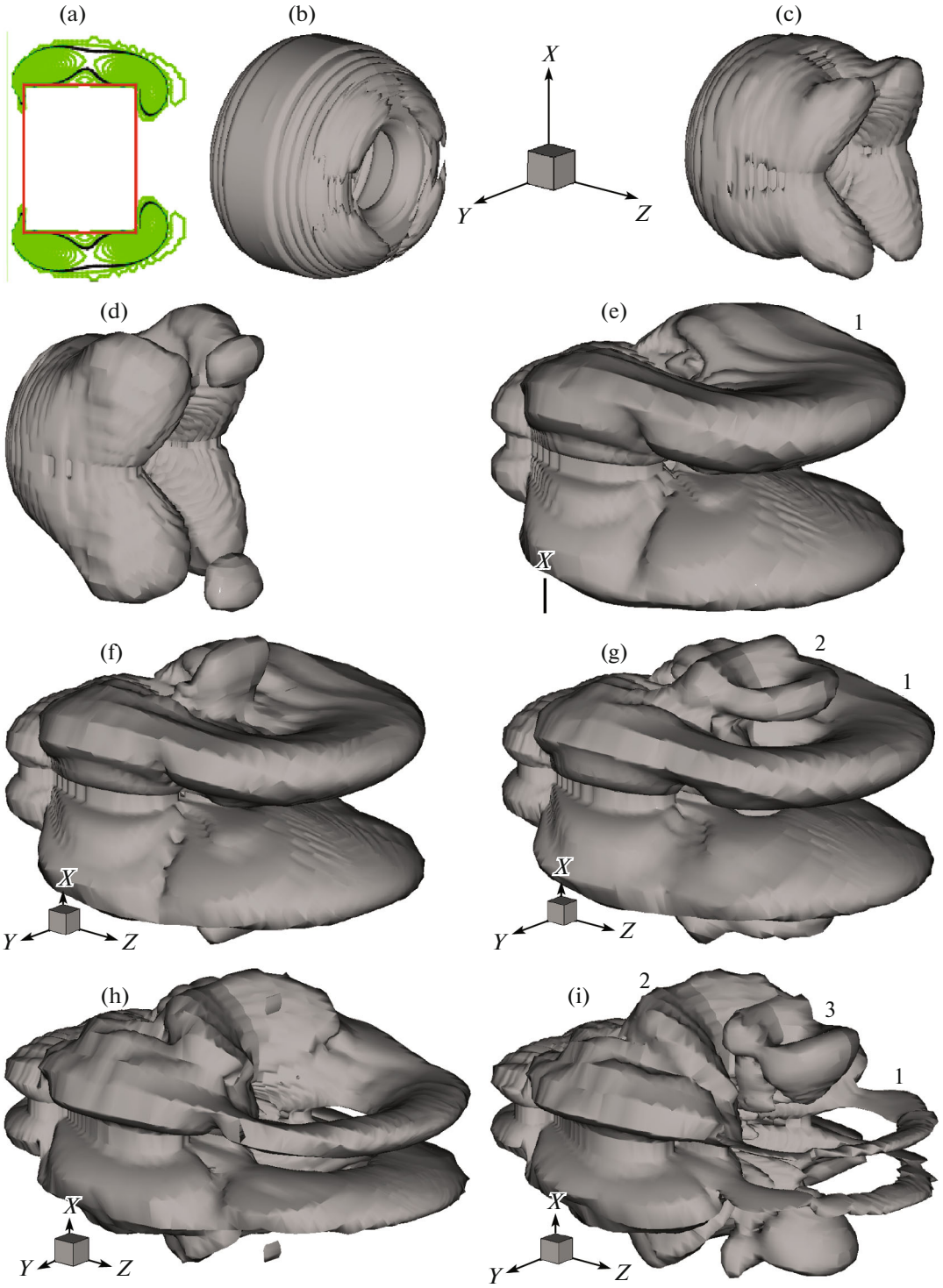

Fig. 6. Flow behind the disk at Fr = 0.5, Re = 50, and A = 981.6: (a) isolines for $\beta > 0$ in the plane $\varphi = \pi/4$ at $T = 0.1$ in steps of 0.1; (b–i) isosurfaces for $\beta = 0.005$ at $T = 0.1$, 0.2, 0.25, 0.7, 0.8, 0.9, 1.3, and 1.5.

between the cells 1 and –1 in the neighborhood of the straight line q (Figs. 5b and 5c(II)). When $0.7 < T \le 0.9$ the deformed vortex ring 2 (Figs. 6f and 6g) is formed around the straight line q (Figs. 5d–5f) owing to the shear and gravitational instabilities. When $0.9 < T \le 1.2$ this ring is displaced downward (closer to point Q) and its left half is transformed into the first crest half-wave (Fig. 6h) (circulation cell 2 in Figs. 5f and 5g). At the same time, the right half of ring 2 (which corresponds to the circulation cell –2 in the

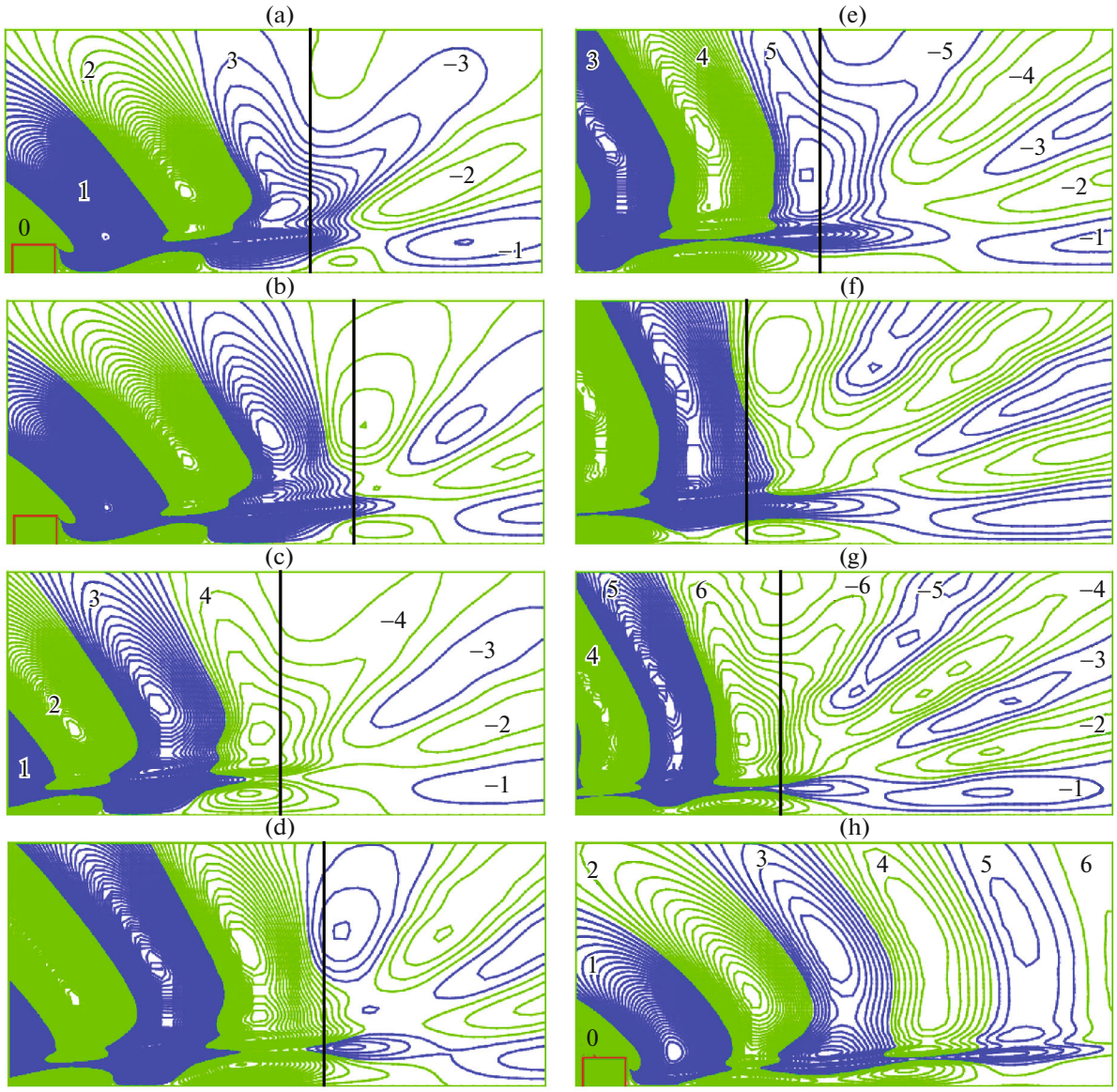

Fig. 7. Flow behind the disk at Fr = 0.5, Re = 50, and A = 981.6 in the plane X–Z: (a–h) $S \times 10^6$ isolines in steps of 2, 2, 2, 1, 1, 0.5, 0.5, and 5 at T = 1.5, 1.75, 2, 2.25, 2.5, 2.75, 3, and 3.

X–Z plane in Fig. 5g) remains in the neighborhood of the straight line q. The velocity of fluid rotation in the circulation cell 2 in Fig. 5g is much higher than in the cell –2; therefore, in Fig. 6h the right half of ring 2 is not seen. When $1.2 < T \le 1.7$ ring 3 is formed and displaced to the Z axis (Figs. 5g–5h and 6h–6i) creating the second hollow half-wave (Figs. 7a and 7b). Thus, when $T > 0.7$ the process of generation of vortex rings (spatial mechanism M2 = {3k}) can be periodically observed above point Q during each $\Delta T = 0.5$. The left halves of the vortex rings are transformed in halves-waves which occupy the space between the disk and point Q. In this case right halves of the rings become thinner with time under pressure of the newborn right halves-waves which press then from above. The universal mechanism M2 works also in the case of the disk at rest.

Figures 5g and 5h (II) clearly demonstrate in detail the way of implementation of the gravitational instability when $1.2 < T \le 1.25$. When $1.1 < T \le 1.15$ vortex-free flow is directed downward in the neighborhood of the straight line q on the boundary between cells 2 and –2. When $T = 1.2$ the velocity along the right boundary $q2$ of the circulation cell 2 inclined at a certain small angle to the vertical becomes a little higher than that near the left boundary of cell –2 due to the fact that the cell 2 is located closer to the disk moving in the second Cartesian coordinate system. The lighter fluid descends along the straight line

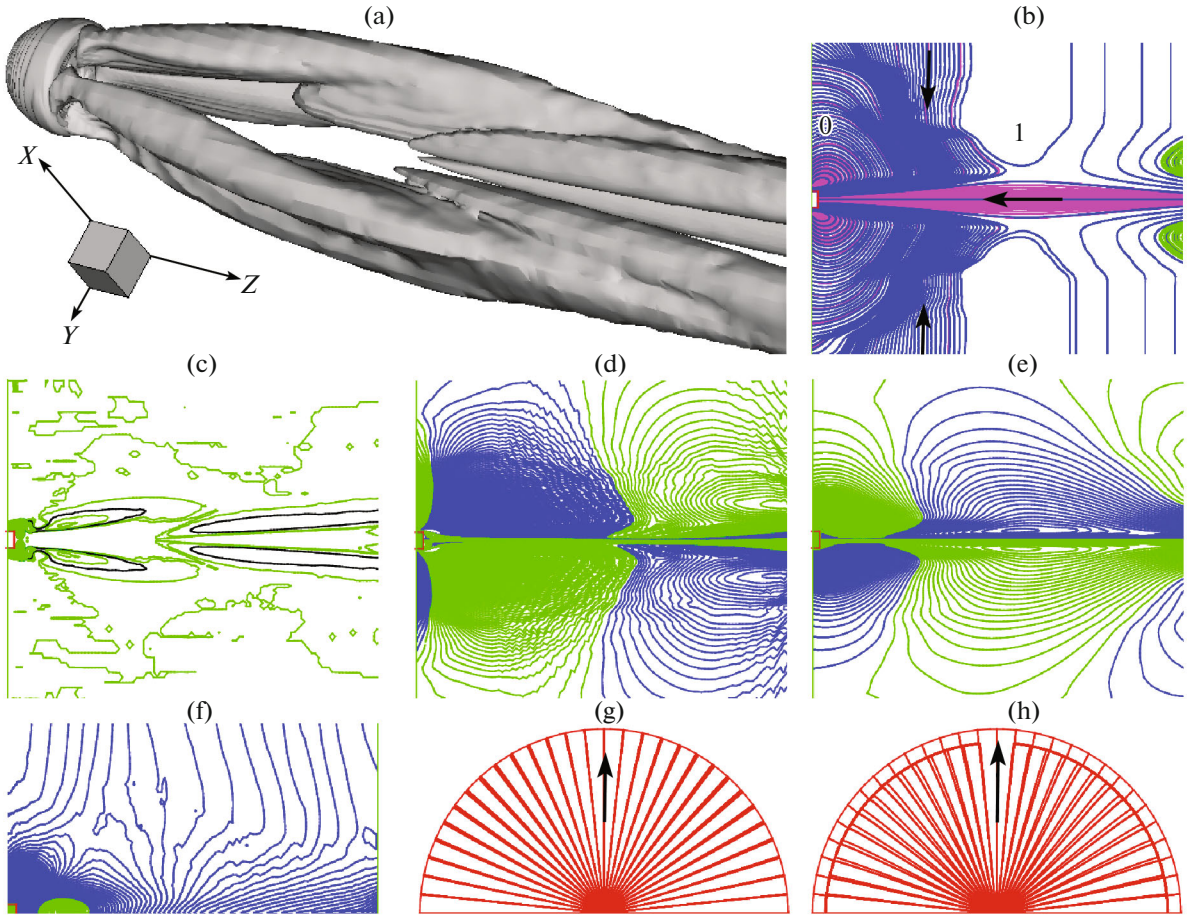

Fig. 8. Time-independent flow behind the disk at Fr = 4.0, Re = 50, A = 2776.4, and $T = 1.2$ ($L/d = 0.729$ and $C_d = 1.89$) in the space (a), in the planes X–Z (b and d–f) and $\varphi = \pi/4$ (c), and on the disk (g–h): (a) isosurface for $\beta = 0.003$; (b) streamlines in the moving Cartesian coordinate system; (c) isolines for $\beta > 0$ in steps of 0.002, (d) S_z-isolines in steps of 5×10^{-8}, (e) S-isolines in steps of 10^{-6}, (f) p-isolines in steps of 10^{-3}; and (g–h) skinfriction patterns on the leading (g) and rear (h) disk surfaces in the stationary Cartesian coordinate system.

$q2$ to the level of the heavier fluid. At the same time, the buoyancy forces tend to return the lighter fluid upward to its level. As a result, when $T = 1.25$ the streamline $q2$ becomes wavy and two small vortices are generated in its neighborhood in the vertical plane X–Z (Fig. 5h (II)). These vortices are two parts of new vortex ring 3 in the space (Fig. 6i) in its cross-section by the plane X–Z. As a result, at $T = 1.25$ ring 3 is generated at "blank" space.

When $T > 0.4$ a certain new cell descends periodically during each $\Delta T = 0.5$ along the straight line q in the S–isoline pattern in the vertical plane X–Z in Figs. 5 (III) and 7. This cell divides the cell beneath it into two cells, namely, the left (new half-wave) and right cells. When $T = 3$, in Figs. 7h–7g we can clearly see cells (halves-waves) 1–5 (to left of q), thinner cells from –1 to –5 (to right of q), and the half divided cell (through which the straight line q passes). From the latter the cells 6 and –6 will be formed at $T = 3.2$. At Fr = 0.5 and Re = 50 the S–isoline patterns are very similar when $T = 3$ and 11.46 (Figs. 7h and 1g), i.e., the three-dimensional vortex structure of internal waves will be approximately the same at $T = 3$ as that shown in Figs. 1b–1c.

We will now turn our attention to the process of formation of flow at Fr = 4 and Re = 50 when $T > 0.72$. In Figs. 3a and 3d we can see the beginning of formation of ring 2 at $T = 0.72$. In Fig. 3b (at the top and bottom) the vortex structure of the first hollow half-wave is similar to a flattened vortex loop whose legs are parallel to the legs of the second pair of vortex loops. When $T > 0.995$ the path passed by the body is equal to $s = 4\pi \mathrm{Fr} T > 50 = z_{\max}$, i.e., in the first (stationary) Cartesian coordinate system the straight line q together with the head of the first loop goes beyond the boundaries of the computational domain. Therefore, at Fr = 4 and Re = 50 in the steady-state flow formed at $T = 1.2$ we can observe only the left halves

of legs of the first pair of vortex loops (Fig. 8a, to the right). At $T = 1.2$ the hollow half-wave 1 occupies almost the entire space between the disk and the right boundary of the computational domain (Figs. 8b–8f). The hollow line can be seen in the pattern of isolines of the pressure perturbations p in the plane X–Z (at the center in Fig. 8f) as in the S_z–isoline pattern in Fig. 8d. The steady-state flow at Fr = 4 and Re = 50 in the neighborhood of the rear disk side is quasi-axisymmetric (Fig. 8h).

SUMMARY

As a result of numerical solution of the system of Navier–Stokes equations in the Boussinesq approximation and visualization of the three-dimensional vortex structure of the flow calculated, the process of formation of three-dimensional internal gravity waves above the point Q of the pulsed start of the center of the rear side of a disk of diameter d and thickness $h = 0.76d$ propagating in the horizontal direction along the axis of disk symmetry Z from right to left in a viscous linearly density-stratified fluid at Fr = 0.5 and 4 and Re = 50 is first considered in detail.

The calculated fields of velocity vectors and pressure perturbations possess the horizontal and vertical planes of symmetry passing through the Z axis. Therefore, the process of flow formation caused by the shear and gravitational instabilities is described in the upper half-space as follows. Initially, two horizontal vortex filaments are formed between the rear disk end face and the point Q of the pulsed start of this end face. Then these filaments are transformed into legs of the hairpin-shaped vortex loop whose head is located to right of Q. Then vortex rings are periodically formed above the point Q during the time interval equal to the half-period of fluid buoyancy. The left halves of these vortex rings are transformed into halves-waves occupying the space between the disk and the point Q. In this case the right halves of the rings become thinner with time under pressure of newborn right semirings pressing on them from above.

The detailed description and the results of analysis of dynamics of formation of three-dimensional vortex structures in a linearly stratified viscous continuum created by disk-shaped objects that move in the horizontal direction are given.

REFERENCES

1. Lighthill, J., *Waves in Fluids*, Cambridge: CUP, 1978.
2. Mitkin, V.V. and Chashechkin, Yu.D., Transformation of hanging discontinuities into vortex systems in a stratified flow behind a cylinder, *Fluid Dynamics*, 2007, vol. 42, no. 1, pp. 12–23.
3. Matyushin, P.V., Evolution of stratified viscous fluid flow in the beginning of motion of a body, *Protsessy v Geosredakh*, 2016, no. 4 (9), pp. 333–343.
4. Chashechkin, Yu.D. and Voeikov, I.V., Vortex systems behind a cylinder in continuously stratified fluid, *Izv. RAN, Fizika Atmosfery i Okeana*, 1993, vol. 29, no. 6, pp. 821–830.
5. Boyer, D.L., Davies, P.A., Fernando, H.J.S., and Zhang, X., Linearly stratified flow past a horizontal circular cylinder, *Phil. Trans. Royal Soc. London. Series A: Math. Phys. Sci.*, 1989, vol. 328, no. 1601, pp. 501–528.
6. Lin, Q., Lindberg, W.R., Boyer, D.L., and Fernando, H.J.S., Stratified flow past a sphere, *J. Fluid Mech.*, 1992, vol. 240, pp. 315–354.
7. Chomaz, J.M., Bonneton, P., and Hopfinger, E.J., The structure of the near wake of a sphere moving horizontally in a stratified fluid, *J. Fluid Mech.*, 1993, vol. 254, pp. 1–21.
8. Boyer, D.L. and Davies, P.A., Laboratory studies of orographic effects in rotating and stratified flows, *Annu. Rev. Fluid Mech.*, 2000, vol. 32, pp. 165–202.
9. Gushchin, V.A. and Matyushin, P.V., Mathematical modeling of the incompressible fluid flows, in *AIP Conference Proceedings*, 2014, vol. 1631, pp. 122–134.
10. Gushchin, V.A. and Matyushin, P.V., Simulation and study of stratified flows around finite bodies, *Computational Mathematics and Mathematical Physics*, 2016, vol. 56, no. 6, pp. 1034–1047.
11. Matyushin, P.V., Classification of the regimes of stratified viscous fluid flows past a disk, *Protsessy v Geosredakh*, 2017, no. 4 (13), pp. 678–687.
12. Hanazaki, H., A numerical study of three-dimensional stratified flow past a sphere, *J. Fluid Mech.*, 1988, vol. 192, pp. 393–419.
13. Baidulov, V.G., Matyushin, P.V., and Chashechkin, Yu.D., Evolution of the diffusion-induced flow over a sphere submerged in a continuously stratified fluid, *Fluid Dynamics*, 2007, vol. 42, no. 2, pp. 255–267.

14. Belotserkovskii, O.M., Gushchin, V.A., and Konshin, V.N., Splitting method for studying stratified fluid flows with free surface, *USSR Computational Mathematics and Mathematical Physics*, 1987, vol. 27, no. 2, pp. 181–196.

15. Matyushin, P.V., *Numerical Simulation of Three-Dimensional Separation Flows of a Homogeneous Incompressible Viscous Fluid past a Sphere*, Thesis of Candidate of Phys.-Math. Sci., Speciality code 05.13.18, Moscow, 2003.

16. Gushchin, V.A. and Matyushin, P.V., Vortex formation mechanisms in the wake behind a sphere for 200 < Re < 380, *Fluid Dynamics*, 2006, vol. 41, no. 5, pp. 795–809.

17. Bobinski, T., Goujon-Durand, S., and Wesfreid, J.E., Instabilities in the wake of a circular disk, *Phys. Rev.,* 2014, vol. E 89, p. 053021.

18. Magarvey, R.H. and Bishop, R.L., Transition ranges for three-dimensional wakes, *Can. J. Phys.*, 1961, vol. 39, pp. 1418–1422.

19. Sakamoto, H. and Haniu, H., A study on vortex shedding from spheres in a uniform flow, *Trans. ASME: J. Fluids Engng.*, 1990, vol. 112, p. 386–392.

Translated by E.A. Pushkar